Electro-osmosis of non-Newtonian fluids in porous media using lattice Poisson–Boltzmann method

Simeng Chen [a,1,2], Xinting He [a,1], Volfango Bertola [b], Moran Wang [a,*]

[a] Department of Engineering Mechanics and CNMM, Tsinghua University, Beijing 100084, China
[b] School of Engineering, University of Liverpool, Liverpool L69 3GH, UK

ABSTRACT

Electro-osmosis in porous media has many important applications in various areas such as oil and gas exploitation and biomedical detection. Very often, fluids relevant to these applications are non-Newtonian because of the shear-rate dependent viscosity. The purpose of this study was to investigate the behaviors and physical mechanism of electro-osmosis of non-Newtonian fluids in porous media. Model porous microstructures (granular, fibrous, and network) were created by a random generation-growth method. The nonlinear governing equations of electro-kinetic transport for a power-law fluid were solved by the lattice Poisson–Boltzmann method (LPBM). The model results indicate that: (i) the electro-osmosis of non-Newtonian fluids exhibits distinct nonlinear behaviors compared to that of Newtonian fluids; (ii) when the bulk ion concentration or zeta potential is high enough, shear-thinning fluids exhibit higher electro-osmotic permeability, while shear-thickening fluids lead to the higher electro-osmotic permeability for very low bulk ion concentration or zeta potential; (iii) the effect of the porous medium structure depends significantly on the constitutive parameters: for fluids with large constitutive coefficients strongly dependent on the power-law index, the network structure shows the highest electro-osmotic permeability while the granular structure exhibits the lowest permeability on the entire range of power law indices considered; when the dependence of the constitutive coefficient on the power law index is weaker, different behaviors can be observed especially in case of strong shear thinning.

© 2014 Elsevier Inc. All rights reserved.

1. Introduction

Electro-osmosis in porous media has broad applications in oil exploration, chemical engineering and biomedical engineering [1–4]. For instance, a better understanding of osmotic behavior of crude oil, especially heavy oil, in geological rocks may help increasing or maintaining production of oil reservoirs [5]. As it is well known, oil cannot be simply regarded to as a Newtonian fluid because of its shear-rate dependent viscosity [6]. As the pore size decreases, the relative importance of surface forces increases significantly. Since crude oils contain many ions, the electrokinetic force is not negligible in osmotic processes. Even though it is not yet a mature technology, electro-osmosis provides a possible option to enhance oil recovery that may be beneficial to the oil and gas industry, because the electrokinetic force is much higher than the shear force in micro/nanoscale flows; in addition, the

absence of moving parts makes this technology extremely reliable. Another important application of the electro-osmosis of non-Newtonian fluids is in microfluidic systems [7,8], such as Lab-on-a-Chip in biomedical applications, integrating various functions including sample detection, separation, mixing and collection. A typical example is electrochromatography in microchips [9]. Since the electrokinetic force at the microscale becomes stronger than pressure from classical mechanical pumps, the system is more reliable because there are no moving parts, and easier to integrate on the chip, this technology is a very promising option of driving and actuating power [10]. Controlling the fluid movements on the chip with precision requires a sound understanding of the hydrodynamics of fluids containing ions under the effects of an electric field; moreover, most of the fluids involved in these applications are non-Newtonian [11], hence the importance of investigating the electro-osmotic flow of non-Newtonian fluids.

There is considerable amount of literature on both theoretical and experimental investigations of electro-osmosis of Newtonian fluids in porous media [2,12–25]. Looker and Carnie [26] proposed a homogenized model upscaling the electrokinetic equations describing transport of a Newtonian solvent through porous med-

* Corresponding author.
  E-mail address: mrwang@tsinghua.edu.cn (M. Wang).
[1] The first two authors contribute equally to this work.
[2] Liverpool University, UK.

ium. Rosanne [27] validated a simple analytic expression for the Newtonian electro-osmosis in compact clays by comparison with both the numerical results of Marino et al. [28] and their own experimental data. Wang et al. developed a lattice Poisson–Boltzmann method (LPBM) [29–31] and investigated the effects of various structures of the porous medium (granular, fibrous, or network) on Newtonian electro-osmotic transport using a computational approach [19,20,24,25].

All of the above mentioned studies focus on Newtonian fluids in porous media. However, the introduction of non-Newtonian effects is important for two main reasons: (i) in electrokinetic flow, the interaction between the fluid and solid surfaces generates a certain amount of net charge on solid surfaces. As a result, the ion distribution across the channel becomes non-uniform, and in particular the ion density near the solid wall is much larger than that in the middle of the channel, so that the electric force imposed on the fluid is non-uniform in the transversal direction. Since the traditional pressure-driven method would result in uniform force on the liquid, some new features are expected in the case that a non-Newtonian fluid is driven by non-uniform force compared with the case of Newtonian fluid. (ii) Porous media naturally set a complex boundary condition for fluid flows; these would influence the flow structure of non-Newtonian fluids significantly. Consequently, investigation of electro-osmosis of non-Newtonian fluids in porous media is of great interest both from the theoretical and from the practical point of view. New findings about the physicochemical properties of electro-osmosis of non-Newtonian fluids in porous media would help understanding this complex transport process further. A deeper understanding of electro-osmosis of non-Newtonian fluids in porous media could enable us to apply theoretical models to practical technology.

Many researchers have recently focused on non-Newtonian fluids flows in porous media [5,32–36]. Lopez et al. [5] used a pore-network model to predict the apparent viscosity of power-law fluids in a porous medium as a function of flow rate. This simulation could reach an agreement with the results of some experiments, but need a highly detailed description of the pores and was limited to a simple rheological model. Boek et al. [33] presented a lattice Boltzmann study of the flow of non-Newtonian fluids, using a power-law relationship between the apparent viscosity and the local shear rate. Their results are in good agreement with theory. However, to date, the research of the electro-osmosis of non-Newtonian fluids in porous media is still at an early stage [37–39]. Mondal and De [39] derived an analytical solution, describing the flow and mass transport behavior of non-Newtonian fluids in a porous microchannel, under the influence of electrokinetic forces. Tang et al. [38] modeled a power-law fluid flow in a two-dimensional porous structure in combination with the electroviscous effect. Two main deficiencies exist in previous studies: (i) for fluid flow in porous media, modeling is reliable only for three-dimensional structures; (ii) either granular microstructures or homogeneous models have been considered so far, however in nature there are various types of porous media microstructures, including granular, fibrous, and network structures [40,41]. To our best knowledge, in the open literature one can find only contributions about the electro-osmosis of non-Newtonian flows in granular porous media, while other microstructures have not been investigated to date.

The primary objective of this work was to investigate the structure effects on electro-osmotic permeability of non-Newtonian fluids through various types of porous media. This article is organized as follows: In Section 2, a theoretical and numerical framework is introduced, including the random generation growth method for microstructure generation, the rheological parameters of non-Newtonian fluids, and a lattice evolution solver for the governing equations; in Section 3, the structure effects on electro-osmosis of non-Newtonian fluids in porous media are analyzed; finally, a brief summary/conclusion is presented in Section 4.

2. Theoretical and numerical framework

2.1. Generation of porous structures

In this work, the multi-parameter random generation-growth method [40] is used to build the microporous structure using statistical information from a real porous medium. The structure generated by this stochastic algorithm features all the relevant characteristics of real porous media. The statistical information used to reproduce microstructures includes the shape and number density of particles, phase volume fraction, morphology, anisotropy, and so on. In general, the solid structures of porous media can be sorted into three categories: granular, fibrous, and network structures.

For different types of microstructures, the generation methods follow the same approach. As an example, the generation procedure of granular porous structure is presented here [19,42]: (1) solid cores are distributed in a three-dimensional grid according to a given core distribution probability c_d. Each point of the grid is assigned a random number between 0 and 1. If the random number is not greater than the distribution probability, the point is chosen as a "seed" of the porous medium. (2) Each solid core is extended toward its neighbor units according to the given direction growth probability D_i (where i represents the direction). Similarly, each direction of the solid core generated in the first step is allocated a random number. If the random number of the i-th direction is smaller than or equal to the direction growth probability D_i, the neighbor unit on the i-th direction becomes a solid core. (3) Repeat the second step until the porosity of the porous structure reaches the given value, ε.

For fibrous porous structures, first fibrous seeds are randomly distributed in the grid system based on the core distribution probability c_d. For each seed, an orientation angle in the range $[-\theta_{\lim}, \theta_{\lim}]$ is assigned stochastically. Then, the length of each fibrous core is extended on both sides along the direction θ; the same is done with the thickness of the fibrous core crosswise. This process is repeated until the fibrous characteristic length meets the given value or the porosity reaches the expected value.

As for to network porous structures, similar to the processes described above seeds are randomly allocated in the grid system according to a given value of core distribution probability, c_d. For each node, a number N_n of neighbor units around the node are randomly chosen as connecting nodes. Here, the value of N depends on certain properties of the expected porous structure, obtained from different generation and search algorithms [43]. Fig. 1(a)–(c) displays the 3D view of sample granular, fibrous and network porous structures generated by the above generation and growth methods, respectively.

2.2. Rheological parameters

In this work, time-independent model non-Newtonian fluids with a shear-rate-dependent viscosity are considered. Such fluids can be described by various constitutive equations, including the power-law (Ostwald–DeWaele) model as well as other complex models (Casson, Herschel-Bulkley, Steiger-Ory, Bingham, Ellis and Eyring) [44]. The power law constitutive equation, can be written as

$$\eta = K\dot{\gamma}^{n-1} \tag{1}$$

where η is the apparent shear viscosity, K is the consistency coefficient, $\dot{\gamma}$ is the shear rate, and n the power-law index; for $n < 1$, the
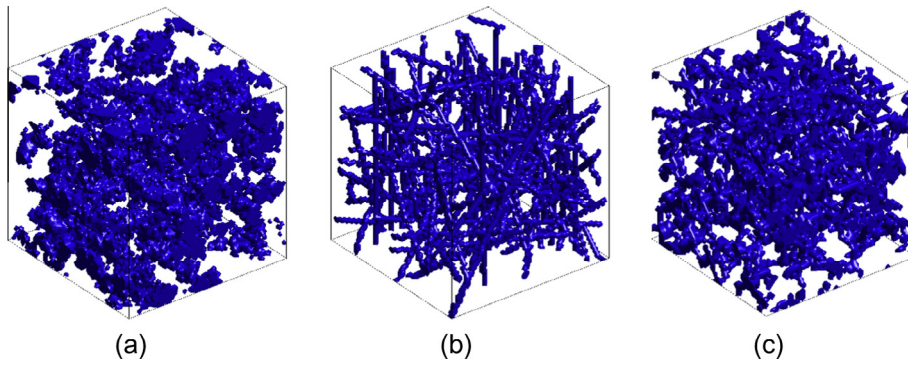
Fig. 1. Porous structures: (a) granular, (b) fibrous and (c) network.

model describes shear-tinning fluids, whereas for $n > 1$ it describes shear-thickening fluids. So far, this model has been the most popular because of its simplicity and ease to use. Thus, the power-law constitutive equation was used in this work to investigate the characteristic behaviors of typical shear-thinning and shear-thickening fluids.

Rheological measurements on real fluids show that when the power-law model is fitted to experimental data, the consistency coefficient and the power-law index are not independent, but are often related by an exponential function as [32,45]:

$$K = A \exp(-B \times n) \quad (2)$$

Fig. 2 shows examples of such fitting curves based on literature data [32,45].

2.3. Governing equations

Consider a dilute non-Newtonian electrolyte solution flowing through a three-dimensional solid porous structure. Although the pore scale may be of tens of nanometers, the non-Newtonian electrolyte can be treated as a continuum fluid since the size is still about one order of magnitude greater than the molecular diameters of the liquid solvent [46].

The mathematical model of electrokinetic transport is based on following assumptions: (i) The system is in a chemical and dynamic equilibrium state; (ii) The transport process is steady; (iii) The characteristic size of pores is much larger than the size of liquid molecules; (iv) The ions in the Stern layer are absorbed to the solid surface rigidly and there is no contribution to bulk ion movement; (v) The flow is slow enough to neglect the effects

of ion convection; (vi) The bulk ion concentration is neither very high (<1 mol/L) nor extremely low (the Debye length is one order of magnitude smaller than the channel width) so that the Poisson–Boltzmann (PB) model is still applicable [46]; (vii) On the solid surface the only chemical processes are chemical adsorption and dissociation; and (viii) difference in dielectric constants between solid frame and liquid solution is negligible. Based on the assumptions of negligible convection effects and moderate ion concentration, the ion transport process could be described by a weak-coupling Poisson–Boltzmann model instead of the strong-coupling Poisson–Nernst–Plank model [7]. The governing equations of electrokinetic transport for a univalent electrolyte solution can be expressed as [7,47]:

$$\nabla^2 \psi = \frac{2en_\infty}{\varepsilon_r \varepsilon_0} \sinh\left(\frac{e\psi}{kT}\right) \quad (3)$$

$$\rho_e = -2en_\infty \sinh\left(\frac{e\psi}{kT}\right) \quad (4)$$

$$\nabla \cdot \mathbf{u} = 0 \quad (5)$$

$$\rho \mathbf{u} \cdot \nabla \mathbf{u} = -\nabla p + \mu \nabla^2 \mathbf{u} + \rho_e \mathbf{E} \quad (6)$$

where ψ denotes the electrostatic potential, e is the absolute value of the proton charge, $\varepsilon_r \varepsilon_0$ is the permittivity of the solution, n_∞ is the bulk ion concentration, k is Boltzmann's constant, T is the absolute temperature, $\mathbf{u}$ is the fluid velocity, ρ is the fluid density, p is the pressure, μ is the dynamic viscosity, ρ_e is the charge density, and $\mathbf{E}$ is the electric field strength. Among the above four equations,
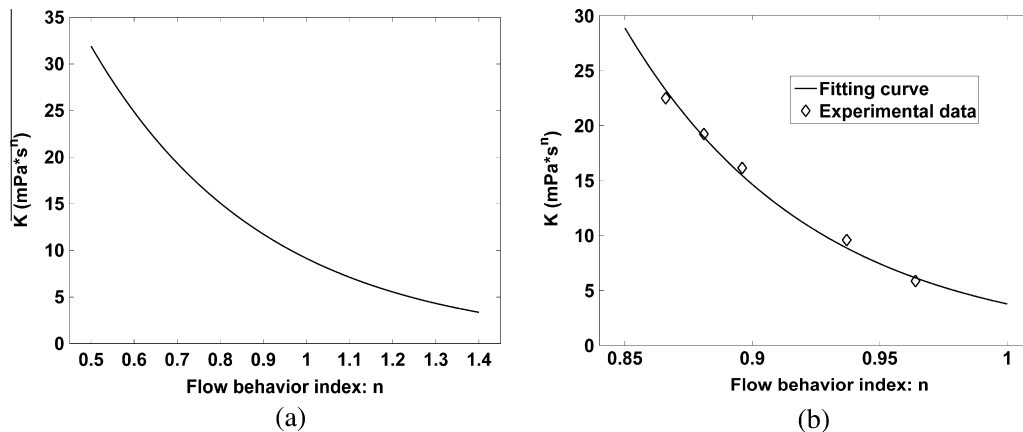
Fig. 2. Examples of fitting curve of rheological parameters power law fluids according to Eq. (2): (a) $A = 111.35$ and $B = 2.5$ for human blood through a capillary viscometer [45]; (b) $A = 3 \times 10^6$ and $B = 13.59$ for foam oil [32].

Eqs. (3) and (4) are the governing equations for the electric potential, while Eqs. (5) and (6) are the evolution equations for hydrodynamics.

2.4. Lattice Poisson–Boltzmann method (LPBM)

After generating the porous medium structure, the lattice Poisson–Boltzmann method (LPBM) was used to solve the coupling governing equations of electric potential and hydrodynamics in electrokinetic transport with bounce-back boundary conditions [29]. This method combines the solution of nonlinear Poisson equations through evolving electric potential on a discrete grid (lattice Poisson method) [48] with the method which solves Boltzmann–BGK equations by evolving density on the same discrete grid (lattice Boltzmann method) [29]. Because previous research indicated that the three-dimension fifteen-speed (D3Q15) scheme in numerical simulation of electro-osmosis in porous media [19] is unstable in cases of high ζ potential and low porosity [49], a more stable three-dimension nineteen-speed (D3Q19) scheme was used to replace the D3Q15 scheme [49].

The discrete evolution equations that solve the governing equations for hydrodynamics (Eqs. (5) and (6)) can be written as [50]

$$f_\alpha(\mathbf{r} + \mathbf{e}_\alpha \delta_t, t + \delta_t) - f_\alpha(\mathbf{r}, t) = -\frac{1}{\tau_v}[f_\alpha(\mathbf{r}, t) - f_\alpha^{eq}(\mathbf{r}, t)] + \delta_t F_\alpha \quad (7)$$

where δ_t is the time step and $\mathbf{e}_\alpha$ is the discrete velocity for the D3Q19 system, which is shown in Fig. 3. The three-dimensional discrete velocities for the D3Q19 system are

$$\mathbf{e}_\alpha = \begin{cases} (0,0,0) & \alpha = 0 \\ (\pm 1, 0, 0)c, (0, \pm 1, 0)c, (0, 0, \pm 1)c & \alpha = 1 \text{ to } 6 \\ (\pm 1, \pm 1, 0)c, (\pm 1, 0, \pm 1)c, (0, \pm 1, \pm 1)c & \alpha = 7 \text{ to } 18 \end{cases} \quad (8)$$

In Eq. (7), τ_v is the dimensionless relaxation time, which depends on the fluid kinematic viscosity, v:

$$\tau_v = 0.5 + 3v/\delta_x c \quad (9)$$

where $c = \delta_x/\delta_t$ is the lattice speed, an adjustable parameter, which controls accuracy and efficiency, and δ_x is the lattice constant (grid size). In previous simulations of electro-osmosis of Newtonian fluids, τ_v was regarded to as a constant. However, in this study τ_v is a shear-rate dependent variable at each node, since the viscosities of non-Newtonian fluids vary with the shear rate. For power-law fluids, the correlation between kinematic viscosity and shear strain tensor can be expressed as

$$v = K\dot{\gamma}^{n-1}/\rho = K(S_{ij}S_{ij})^{(n-1)/2}/\rho \quad (10)$$
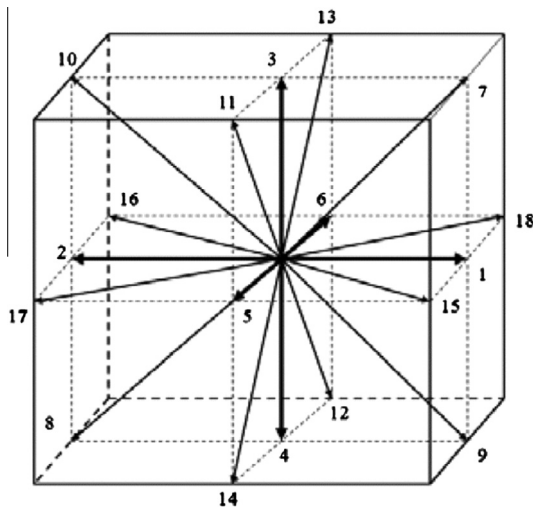
Fig. 3. Lattice direction system in the D3Q19 model.

where K is the consistency (Pa s^n), $\dot{\gamma}$ is the shear rate (s^{-1}), S_{ij} is the strain rate tensor, and ρ is the fluid density.

Artoli [51] derived the formula for calculating the shear strain tensor using non-equilibrium distribution function

$$S_{ij} = -\frac{3}{2\rho c^2 \tau_v} \sum_\alpha f_\alpha^{(1)} c_{\alpha i} c_{\alpha j} \quad (11)$$

where $f_\alpha^{(1)}$ is the first order term of the non-equilibrium distribution function. Since high order ($\geqslant 2$) terms are infinitesimals compared to the first order term, we approximately regard the whole non-equilibrium distribution function as the first order non-equilibrium distribution function

$$f_\alpha^{(1)} \approx f_\alpha^{neq} = f_\alpha - f_\alpha^{eq} \quad (12)$$

Combining Eqs. (9)–(12), one can derive a shear-dependent relaxation time τ_v with density distribution functions at each node. The above procedure allows one to incorporate the power-law constitutive model into the LPBM.

The density equilibrium function f_α^{eq} in the D3Q19 model can be calculated as

$$f_\alpha^{eq} = \omega_\alpha \rho \left[1 + 3\frac{\mathbf{e}_a \cdot \mathbf{u}}{c^2} + 9\frac{(\mathbf{e}_a \cdot \mathbf{u})^2}{2c^2} - \frac{3\mathbf{u}^2}{2c^2} \right] \quad (13)$$

with

$$\omega_\alpha = \begin{cases} 1/3 & \alpha = 0 \\ 1/18 & \alpha = 1 \text{ to } 6 \\ 1/36 & \alpha = 7 \text{ to } 18 \end{cases} \quad (14)$$

The external force in Eq. (7) is [52]

$$F_\alpha = \frac{3\rho_e \mathbf{E} \cdot (\mathbf{e}_\alpha - \mathbf{u})}{\rho c^2} f_\alpha^{eq} \quad (15)$$

The macro fluid density and velocity can be calculated by [19,41]

$$\rho = \sum_\alpha f_\alpha \quad (16)$$

$$\rho \mathbf{u} = \sum_\alpha \mathbf{e}_\alpha f_\alpha \quad (17)$$

Similarly, the discrete evolution equation for electric potential distribution takes the form [29,48]

$$g_\alpha(\mathbf{r} + \Delta\mathbf{r}, t + \delta_{t,g}) - g_\alpha(\mathbf{r}, t) = -\frac{1}{\tau_g}[g_\alpha(\mathbf{r}, t) - g_\alpha^{eq}(\mathbf{r}, t)] + \left(1 - \frac{0.5}{\tau_g}\right)\delta_{t,g}\omega_\alpha g_s \quad (18)$$

where the equilibrium distribution function of the electric potential evolution variable g in the D3Q19 model is

$$g_\alpha^{eq} = \begin{cases} 0 & \alpha = 0 \\ \psi/18 & \alpha = 1 \text{ to } 6 \\ \psi/18 & \alpha = 7 \text{ to } 18 \end{cases} \quad (19)$$

The time step for electric potential evolution is $\delta_{t,g} = \delta_x/c_g$, where c_g is the lattice speed for electric potential propagation [48]. The dimensionless relaxation time can be obtained through a multi-scale analysis of the discrete Boltzmann evolution equations. For the D3Q19 model [49,53], it can be expressed as

$$\tau_g = \frac{9\chi}{5\delta_x c_g} + 0.5 \quad (20)$$

where χ is defined as the electric potential diffusivity and is set to unity in these simulations. The variable c_g is also an adjustable parameter that forces the value of τ_g to be within the range between 0.5 and 2 [48,54]. The macro electric potential can be calculated by
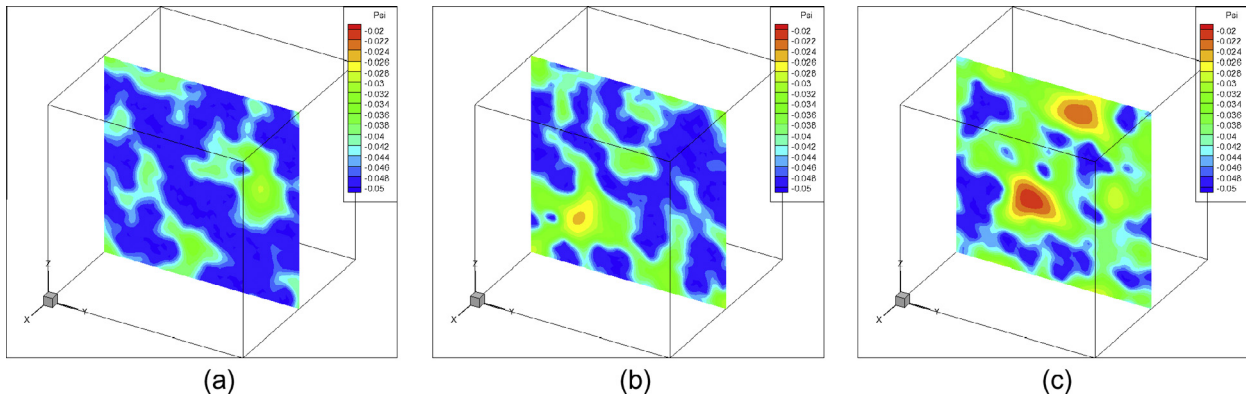
Fig. 4. Electric potential contours on the mid-plane (x direction) of granular porous structures at porosities $\varepsilon = 0.45$, $\varepsilon = 0.63$, and $\varepsilon = 0.73$ respectively.

$$\psi = \sum_{\alpha}(g_{\alpha} + 0.5\delta_{t}g_{s}\omega_{\alpha}) \tag{21}$$

As for the boundary conditions for the lattice Boltzmann equations, the non-equilibrium bounce-back rule [55] was applied to both hydrodynamic and electrodynamic boundaries. For the hydrodynamic boundaries, it can be written as: $f_{\alpha}^{neq} = f_{\beta}^{neq}$, where the subscripts α and β represent the opposite directions. For the electric potential at solid surfaces, the non-equilibrium "bounce-back" rule is derived as $g_{\alpha}^{neq} = -g_{\beta}^{neq}$. These current boundary conditions have approximately second-order accuracy [53,55].

3. Simulation results and discussion

In order to study the structure effect of electro-osmosis in porous media, first a given type of microporous structure (granular, fibrous, or network) is generated, then the governing equations for electrokinetic transport are solved by the lattice Poisson–Boltzmann method. Once the whole velocity field has been obtained, the electro-osmotic permeability is defined as $\kappa_{e} = \bar{u}/E$ [56], where $\bar{u}$ is the average fluid velocity in the direction of external electric field **E**.

In these numerical simulations, the computational domain is represented by a micro cube with a side length of 1×10^{-6} m, which is divided into a $60 \times 60 \times 60$ uniform grid. The fluid properties are the fluid density $\rho = 1 \times 10^{3}$ kg/m³, and the dielectric constant $\varepsilon_{r}\varepsilon_{0} = 6.95 \times 10^{-10}$ C²/J m [29]. The values of the consistency coefficient K and the flow behavior index n are adjusted to obtain shear-thinning and shear-thickening behaviors, as discussed in Section 2.2. Unless otherwise specified, the other parameters are the absolute temperature, $T = 293$ K, the zeta potential, $\zeta = -50$ mV, the bulk ion concentration, $n_{\infty} = 1 \times 10^{-5}$ mol/L, and the external electric field strength, $E = 1 \times 10^{8}$ V/m.

Figs. 4(a)–(c) displays the electric potential contours in the mid-plane (x direction) of granular porous structures with porosities 0.45, 0.63, and 0.73 respectively. Since the boundary condition on the solid nodes is set to zeta potential $\zeta = -0.05$ V, the darkest color (blue)[1], i.e. where the absolute value of the electric potential is highest, corresponds to the solid phase. These three figures use the same color-map in order to visualize the differences among the development of surface electric potential at different porosities.

3.1. External electric field strength effect

Fig. 5 displays the electro-osmotic permeability, κ_{e}, as a function of the external electric field strength, E_{x}, for three kinds of

___
[1] For interpretation of color in Fig. 4, the reader is referred to the web version of this article.

power law fluids with different rheological properties (respectively shear-thinning, $n = 0.8$, Newtonian, $n = 1.0$, and shear thickening, $n = 1.2$). The microstructure of the porous medium is granular, with a porosity $\varepsilon = 0.18$. From Fig. 5, one can notice that for Newtonian fluids the electro-osmotic permeability remains constant with the increase of the external electric field. In other words, the average fluid velocity along the direction of the external electric field is a linear function of the external electric field strength. This result is in agreement with the expression of the H–S (Helmholtz–Smoluchowski) velocity for Newtonian fluids

$$\mathbf{u}_{slip} = -\frac{\varepsilon_{0}\varepsilon_{r}\zeta\mathbf{E}}{\mu} \tag{22}$$

As shown in Fig. 5, the electro-osmotic permeability is almost linear with respect to the external electric field for both shear-thinning and shear-thickening fluids. The slope for shear-thinning fluids is positive while the slope for shear-thickening is negative. For a low external electric field, the shear-thickening fluid exhibits the highest electro-osmotic permeability while the shear-thinning fluid results in the lowest electro-osmotic permeability, and vice-versa for high electric fields. In fact, the relationship between the average fluid velocity in the direction of the external electric field and external electric field strength, illustrated in figure, is consistent with the formula to calculate the H–S velocity of non-Newtonian fluids obtained by Zhao et al. [57]

$$u_{s} = n\kappa^{\frac{1-n}{n}}\left(-\frac{\varepsilon_{r}\varepsilon_{0}\zeta E_{x}}{K}\right)^{\frac{1}{n}} \tag{23}$$

Eq. (23) can be rewritten as

$$\frac{u_{s}}{E_{x}} = n\kappa^{\frac{1-n}{n}}\left(-\frac{\varepsilon_{r}\varepsilon_{0}\zeta}{K}\right)^{\frac{1}{n}}E_{x}^{\frac{1}{n}-1} \tag{24}$$

According to Eq. (24), when the flow behavior index n is equal to 1 (Newtonian fluid), the ratio u_{s}/E_{x} (electro-osmotic permeability) does not change with the external electric field strength E_{x}. In case of $n < 1$ (shear-thinning fluid), u_{s}/E_{x} increases linearly with E_{x}, while in the case of $n > 1$ (shear-thickening fluid), u_{s}/E_{x} decreases linearly with E_{x}.

3.2. Zeta potential effect

Fig. 6 shows the electro-osmotic permeability κ_{e} as a function of the zeta potential, ζ, for three power law fluids (shear-thinning $n = 0.8$, Newtonian $n = 1$, and shear thickening $n = 1.2$) in a granular porous medium with porosity $\varepsilon = 0.18$ and external electric field $E_{x} = 1 \times 10^{8}$ V/m. Logarithmic coordinates were used for the y-axis since the electro-osmotic permeability increases by several orders
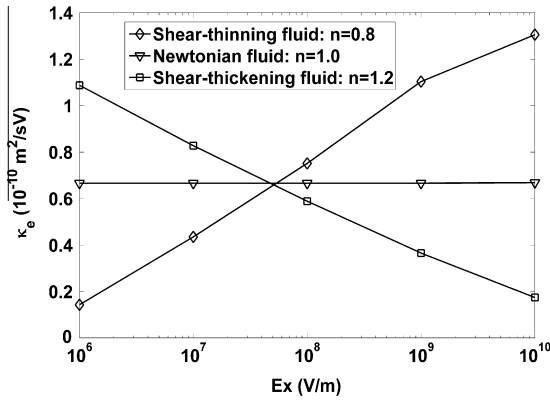
Fig. 5. Electro-osmotic permeability as a function of external electric field strength for three power law fluids (shear-thinning, $n = 0.8$; Newtonian, $n = 1.0$; shear thickening, $n = 1.2$).

Fig. 7. Electro-osmotic permeability as a function of the bulk ion concentration for three power law fluids (shear-thinning, $n = 0.8$; Newtonian, $n = 1.0$; shear thickening, $n = 1.2$).
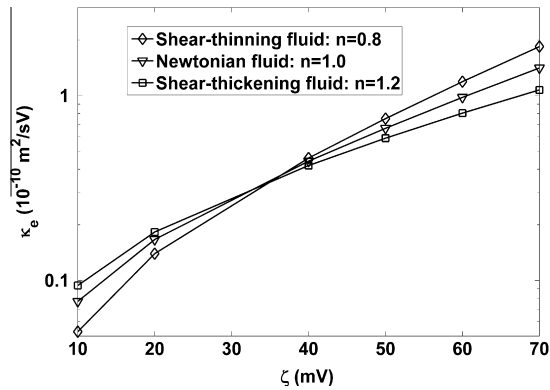
Fig. 6. Electro-osmotic permeability as a function of zeta potential for three power law fluids (shear-thinning, $n = 0.8$; Newtonian, $n = 1.0$; shear thickening, $n = 1.2$).

of magnitude. Fig. 6 suggests that the logarithm of the electro-osmotic permeability is approximately a linear function of the zeta potential for shear-thinning, Newtonian, and shear thickening fluids. In the case of low zeta potential, the shear-thickening fluid exhibits the highest electro-osmotic permeability, while the shear-thinning fluid has the lowest electro-osmotic permeability. However, in case of high zeta potential, the situation is just the opposite (highest electro-osmotic permeability: shear-thinning fluid; lowest electro-osmotic permeability: shear-thickening fluid). This is similar to the behavior of the electro-osmotic permeability with respect to the external electric field (Fig. 5).

3.3. Bulk ion concentration effect

Fig. 7 shows the electro-osmotic permeability κ_e as a function of the bulk ion concentration n_b for three power law fluids (shear-thinning $n = 0.8$, Newtonian $n = 1$, and shear thickening $n = 1.2$) in a granular porous medium with porosity $\varepsilon = 0.18$ and external electric field $E_x = 1 \times 10^8$ V/m. According to Fig. 7, the logarithm of the electro-osmotic permeability is almost linear with respect to the logarithm of the bulk ion concentration for all of the fluids considered, and the overall trends of permeability are qualitatively similar to the previous cases. In fact, shear thickening fluids exhibit the highest permeability at low bulk ion concentrations, and the lowest at high bulk ion concentrations; vice-versa, shear thinning fluids exhibit the lowest permeability at low bulk ion concentrations, and the highest at high bulk ion concentrations.

To understand why the behavior of permeability with respect to the three parameters considered above (external electric field
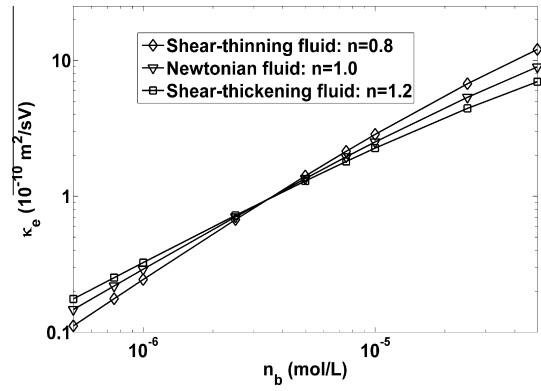
strength, zeta potential, and bulk ion concentration) is qualitatively similar for all cases, one should recognize that all of these parameters can be regarded to as driving factors in the electrokinetic transport. Since the porous structures of the flow field are the same, a large average fluid velocity yields large shear rates $\dot{\gamma}$. According to the power law model (Eq. (1)), the apparent viscosity of power-law fluids depends on the competition between two quantities: the consistency coefficient, K, and the term $\dot{\gamma}^{n-1}$, which can be regarded to as a non-linear shear rate depending on the power law index, n. The consistency coefficient K of shear-thinning fluid is relatively higher than that of shear-thickening fluids, as shown by Eq. (2) and Fig. 2; thus, a very large value of $\dot{\gamma}^{n-1}$, driven by the average fluid velocity, would reduce the apparent viscosity significantly because $n < 1$. As a result, shear-thinning fluids exhibit higher electro-osmotic permeability when the driving factors are relatively strong. In the case of weak driving factors, the average fluid velocity is low therefore the term $\dot{\gamma}^{n-1}$ is small, therefore the apparent viscosity of shear-thinning fluid is high. The picture is very different for shear-thickening fluids, because their consistency coefficient is considerably smaller than that of shear-thinning fluids, and so is the apparent viscosity. As a consequence, shear-thickening fluids exhibit higher electro-osmotic permeability when the driving factors are relatively weaker.

3.4. Porosity effect

Figs. 8 and 9 display the electro-osmotic permeability, κ_e, as a function of porosity ε for the three power-law fluids considered, in a porous medium with granular structure. The magnitudes of the external electric field are $E_x = 1 \times 10^8$ V/m (Fig. 8) and $E_x = 1 \times 10^7$ V/m (Fig. 9). In general, the electro-osmosis grows monotonically with increasing porosity; in the case of high external electric potential ($E_x = 1 \times 10^8$ V/m), shear-thinning fluids exhibit the highest electro-osmotic permeability for any value of porosity, while the opposite situation occurs with a comparatively lower electric potential ($E_x = 1 \times 10^7$ V/m), as shown in Fig. 9. This conclusion is consistent with the common features of electro-osmotic permeability trends with respect to different parameters described above.

3.5. Effect of structure morphology

Figs. 10 and 11 show the effect of the porous medium structure (granular, fibrous, and network) with identical porosity, $\varepsilon = 0.18$, on the electro-osmotic permeability, κ_e, plotted as a function of the flow behavior index, n, respectively for two power law fluids with different constitutive parameters, subject to an electric field
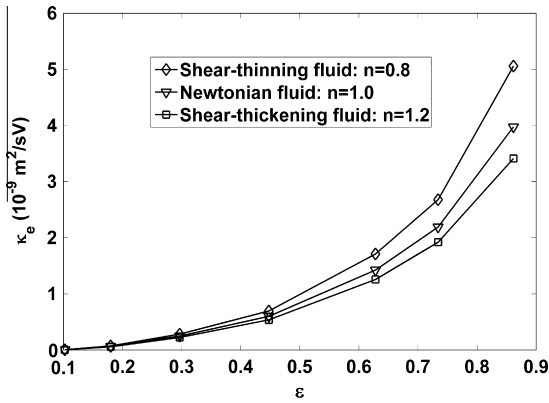
Fig. 8. Electro-osmotic permeability as a function of porosity for three power law fluids (external electric field: $E_x = 1 \times 10^8$ V/m).
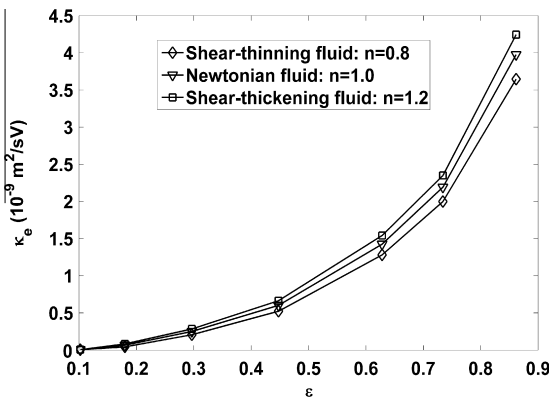
Fig. 9. Electro-osmotic permeability as a function of porosity for three power law fluids (external electric field $E_x = 1 \times 10^7$ V/m).

with magnitude $E_x = 1 \times 10^8$ V/m. In particular, Fig. 10 shows the behavior of a fluid with constitutive parameters related by the following equation:

$$K = 3 \times 10^6 \exp(-13.56 \times n) \qquad (25)$$

whereas Fig. 11 is relative to a fluid with

$$K = 111.35 \exp(-2.5 \times n) \qquad (26)$$

In both cases, the electro-osmotic permeability reduces monotonically when the flow behavior index in all cases. For a fluid with a constitutive coefficient described by Eq. (25) (Fig. 10), the
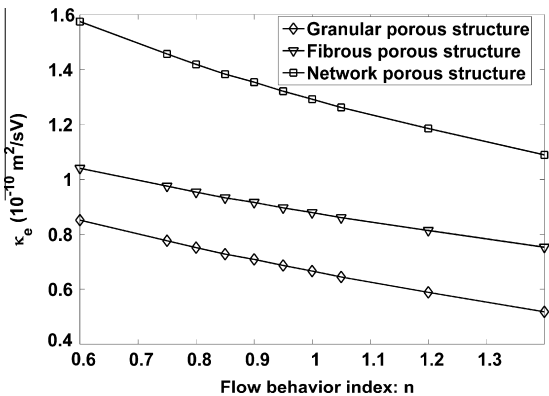
Fig. 10. Electro-osmotic permeability as a function of the flow behavior index for a power law fluid with $K = 3 \times 10^6 \exp(-13.59 \times n)$, for three different porous structures (granular, fibrous, and network).
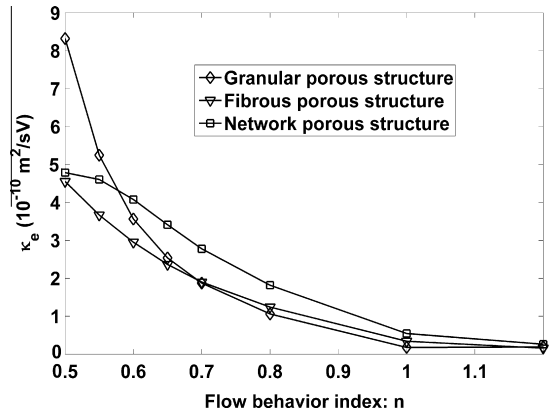
Fig. 11. Electro-osmotic permeability as a function of the flow behavior index for a power law fluid with $K = 111.35 \exp(-2.5 \times n)$, for three different porous structures (granular, fibrous, and network).

network porous structure exhibits the highest electro-osmotic permeability, while the granular porous structure has the lowest permeability at any value of flow behavior index. This is mainly due to the low porosity of porous structures chosen in the simulations. At low porosities, the network structure has the highest surface–volume ratio therefore the area of Electric Double Layers (EDLs) driving the fluid per unit volume is largest. Thus, the network porous structure exhibits the highest electro-osmotic permeability, because it can provide the largest electrokinetic force per volume unit. On the contrary, the granular porous structure exhibits the lowest electro-osmotic permeability since its surface–volume ratio is the lowest. The change of viscosity with the power law index is not significant, because it is compensated by a strong reduction of the consistency coefficient (Eq. (25)).

Fig. 11 shows that for a different choice of the power law parameters (Eq. (26)) the granular porous structure exhibits the highest electro-osmotic permeability when the flow behavior index is below 0.6. The physical reasons for this are to be found in the weaker dependence of the consistency coefficient K on the power law index n, so that there is a strong reduction of the apparent viscosity at low values of n. The region of fully-developed slip velocity (H–S velocity) in the granular porous structure is larger than that in the other two porous structures due a lowest shape resistance. As a result, the granular porous structure exhibits the highest electro-osmotic permeability at low values of the power law index. However, when the flow behavior index exceeds 0.7, the effect of the porous medium structure on electro-osmosis of this fluid becomes consistent with that of the fluid considered previously (i.e. highest electro-osmotic permeability for the network structure, and lowest electro-osmotic permeability for the granular structure). This happens because the electrokinetic transport enhancement caused by the high surface–volume ratio outweighs the expansion of the slip-velocity region resulting from the granular structure due to a weak shear-thinning effect.

4. Conclusions

The electro-osmosis of power-law non-Newtonian fluids in porous media was investigated numerically using a lattice Poisson–Boltzmann approach, for different microstructures of the porous medium (granular, fibrous, or network). The electro-osmotic characteristics of non-Newtonian flows in porous media were analyzed for both shear-thinning and shear-thickening fluids, for different values of the power-law parameters. The correlations between microstructure and electro-osmotic permeability, affected by the fluid properties, are mainly concerned. From these results, one can conclude that:

(1) The electro-osmotic permeability of Newtonian fluid does not vary with the increase of the external electric field magnitude. However, when the external electric field magnitude is increased the electro-osmotic permeability of shear-thinning fluid grows, while that of shear-thickening fluids decreases. In case of low external electric field, the shear-thickening fluid exhibits the highest electro-osmotic permeability, whereas the shear-thinning fluid has the highest electro-osmotic permeability at high values of the electric field.

(2) For a low bulk ion concentration, or zeta potential, the shear-thickening fluid exhibits the highest electro-osmotic permeability, while for a high bulk ion concentration or zeta potential the shear-thinning fluid has the highest electro-osmotic permeability.

(3) The electro-osmotic permeability grows monotonically with the increase of porosity. In case of strong driving factors (external electric field strength, bulk ion concentration, or zeta potential), the shear-thinning fluid exhibits the highest electro-osmotic permeability at all values of porosities. However, in case of weak driving factors, the shear-thickening fluid exhibits the highest electro-osmotic permeability independently of the value of porosity.

(4) For fluids with large consistency coefficients strongly dependent on the power law index, the network and the granular structures exhibit the highest and the lowest electro-osmotic permeability, respectively, on the whole range of power law indices. However, if the fluid consistency coefficient has a weaker dependence on the power laws index, different behaviors can be observed, especially for low values of the power law index.

Since electro-osmosis of non-Newtonian fluid in porous media has so many important applications in energy and environmental fields, this study may improve understanding of mechanism of such a complicated transport process. A few promising future work include extensions to other non-Newtonian fluid than the power-law fluids, such as the Bingham fluid, and to multiphase flow considering liquid–liquid interfaces and displacements.

Acknowledgments

References

[1] A.E. Alexander, P. Jonson, Colloid Science, Clarendon, Oxford, 1949.
[2] K.P. Tikhomolova, Electro-Osmosis, Ellis Horwood, New York, 1993.
[3] J.H. Masliyah, S. Bhattacharjee, Electrokinetic and Colloid Transport Phenomena, Wiley, New York, 2006.
[4] R.E. Oosterbroek, A.v.D. Berg, Lob-on-a-Chip: Miniaturized Systems for (Bio) Chemical Analysis and Sintesis, Elsevier, Boston, 2003.
[5] X. Lopez, P.H. Valvatne, M.J. Blunt, J. Colloid Interface Sci. 264 (1) (2003) 256–265.
[6] M.T. Ghannam, S.W. Hasan, B. Abu-Jdayil, N. Esmail, J. Petrol. Sci. Eng. 81 (2012) 122–128.
[7] D.Q. Li, Electrokinetics in Microfluidics, Academic, Oxford, 2004.
[8] T.M. Squires, S.R. Quake, Rev. Mod. Phys. 77 (3) (2005) 977–1026.
[9] D.J. Throckmorton, T.J. Shepodd, A.K. Singh, Anal. Chem. 74 (4) (2002) 784–789.
[10] C.H. Chen, J.G. Santiago, J. Microelectromech. Syst. 11 (6) (2002) 672–683.
[11] M.A. Hussain, S. Kar, R.R. Puniyani, J. Biosci. 24 (3) (1999) 329–337.
[12] D. Coelho, M. Shapiro, J.F. Thovert, P.M. Adler, J. Colloid Interface Sci. 181 (1) (1996) 169–190.
[13] S. Marino, D. Coelho, S. Bekri, P.M. Adler, J. Colloid Interface Sci. 223 (2) (2000) 292–304.
[14] S. Yao, J.G. Santiago, J. Colloid Interface Sci. 268 (1) (2003) 133–142.
[15] S. Yao, D.E. Hertzog, S. Zeng, J.C. Mikkelsen Jr., J.G. Santiago, J. Colloid Interface Sci. 268 (1) (2003) 143–153.
[16] Y.J. Kang, C. Yang, X.Y. Huang, Int. J. Eng. Sci. 42 (19–20) (2004) 2011–2027.
[17] M.Z. Bazant, T.M. Squires, Phys. Rev. Lett. 92 (6) (2004) 066101.
[18] J.F. Dufrêche, V. Marry, N. Malíková, P. Turq, J. Mol. Liq. 118 (1–3) (2005) 145–153.
[19] M. Wang, S. Chen, J. Colloid Interface Sci. 314 (1) (2007) 264–273.
[20] M. Wang, N. Pan, J.K. Wang, S.Y. Chen, Commun. Comput. Phys. 2 (6) (2007) 1055–1070.
[21] M. Wang, J. Wang, S. Chen, N. Pan, J. Colloid Interface Sci. 304 (1) (2006) 246–253.
[22] A.K. Gupta, D. Coelho, P.M. Adler, J. Colloid Interface Sci. 303 (2) (2006) 593–603.
[23] M. Rosanne, M. Paszkuta, P.M. Adler, J. Colloid Interface Sci. 297 (1) (2006) 353–364.
[24] M. Wang, Q.J. Kang, H. Viswanathan, B.A. Robinson, J. Geophys. Res.-Solid Earth 115 (B10) (2010).
[25] M.R. Wang, J. Heat Transfer-Trans. ASME 134 (5) (2012) 051020.
[26] J.R. Looker, S.L. Carnie, Transport. Porous Media 65 (1) (2006) 107–131.
[27] M. Rosanne, Geophys. Res. Lett. 31 (18) (2004).
[28] S. Marino, M. Shapiro, P.M. Adler, J. Colloid Interface Sci. 243 (2) (2001) 391–419.
[29] J. Wang, M. Wang, Z. Li, J. Colloid Interface Sci. 296 (2) (2006) 729–736.
[30] J.K. Wang, M.R. Wang, Z.X. Li, Mod. Phys. Lett. B 19 (28–29) (2005) 1515–1518.
[31] M.R. Wang, J.K. Wang, S.Y. Chen, J. Comput. Phys. 226 (1) (2007) 836–851.
[32] Y.Q. Long, W.Y. Zhu, J. Li, X.H. Huang, in: Rheological Properties Studies on the Steam-foam Drive in Heavy Oil Reservoirs, Computer Distributed Control and Intelligent Environmental Monitoring (CDCIEM), 2012 International Conference on, 5–6 March 2012, 2012, pp. 600–605.
[33] E.S. Boek, J. Chin, P.V. Coveney, Int. J. Mod. Phys. B 17 (1–2) (2003) 99–102.
[34] C. Migliorini, Y. Qian, H. Chen, E.B. Brown, R.K. Jain, L.L. Munn, Biophys. J. 83 (4) (2002) 1834–1841.
[35] J.R.A. Pearson, P.M.J. Tardy, J. Nonnewtonian Fluid Mech. 102 (2) (2002) 447–473.
[36] V. Bertola, E. Cafaro, Int. J. Heat Mass Transfer 49 (2006) 4003–4012.
[37] C. Zhao, C. Yang, Adv. Colloid Interface Sci. 201–202 (2013) 94–108.
[38] G.H. Tang, J. Nonnewtonian Fluid Mech. 166 (14–15) (2011) 875–881.
[39] S. Mondal, S. De, Electrophoresis 34 (5) (2013) 668–673.
[40] M. Wang, N. Pan, Mater. Sci. Eng. R-Rep. 63 (1) (2008) 1–30.
[41] M. Wang, J. Heat Transfer 134 (5) (2012) 051020.
[42] M. Wang, N. Pan, J. Wang, S. Chen, J. Colloid Interface Sci. 311 (2) (2007) 562–570.
[43] M. Wang, N. Pan, Int. J. Heat Mass Transfer 51 (5–6) (2008) 1325–1331.
[44] G. Bylund, Dairy processing handbook, Tetra Pak Processing Systems AB, 2003.
[45] G.N. Marinakis, J.C. Barbenel, S.G. Tsangaris, Proc. Inst. Mech. Eng. H 216 (6) (2002) 385–392.
[46] M. Wang, S.Y. Chen, Commun. Comput. Phys. 3 (5) (2008) 1087–1099.
[47] R. Schoch, J. Han, P. Renaud, Rev. Mod. Phys. 80 (3) (2008) 839–883.
[48] J.K. Wang, M. Wang, Z.X. Li, Commun. Nonlinear Sci. Numer. Simul. 13 (3) (2008) 575–583.
[49] M. Wang, Q. Kang, Anal. Chem. 81 (8) (2009) 2953–2961.
[50] S. Chen, G.D. Doolen, Annu. Rev. Fluid Mech. 30 (1998) 329–364.
[51] A.M. Artoli, Mesoscopic Computational Haemodynamics, University of Amsterdam, 2003.
[52] X. He, S. Chen, G.D. Doolen, J. Comput. Phys. 146 (1) (1998) 282–300.
[53] M. Rohde, D. Kandhai, J. Derksen, H. Van den Akker, Phys. Rev. E 67 (6) (2003).
[54] J.K. Wang, M. Wang, Z.X. Li, Int. J. Therm. Sci. 46 (3) (2007) 228–234.
[55] Q. Zou, X. He, Phys. Fluids 9 (6) (1997) 1591.
[56] R.P. Rastogi, K.M. Jha, J. Phys. Chem. 70 (4) (1966) 1017–1024.
[57] C. Zhao, E. Zholkovskij, J.H. Masliyah, C. Yang, J. Colloid Interface Sci. 326 (2) (2008) 503–510.